

Inherent toughness and fracture mechanisms of refractory transition-metal nitrides via density-functional molecular dynamics

Davide Sangiovanni

The self-archived postprint version of this journal article is available at Linköping University Institutional Repository (DiVA):

<http://urn.kb.se/resolve?urn=urn:nbn:se:liu:diva-148240>

N.B.: When citing this work, cite the original publication.

Sangiovanni, D., (2018), Inherent toughness and fracture mechanisms of refractory transition-metal nitrides via density-functional molecular dynamics, *Acta Materialia*, 151, 11-20.
<https://doi.org/10.1016/j.actamat.2018.03.038>

Original publication available at:

<https://doi.org/10.1016/j.actamat.2018.03.038>

Copyright: Elsevier

<http://www.elsevier.com/>



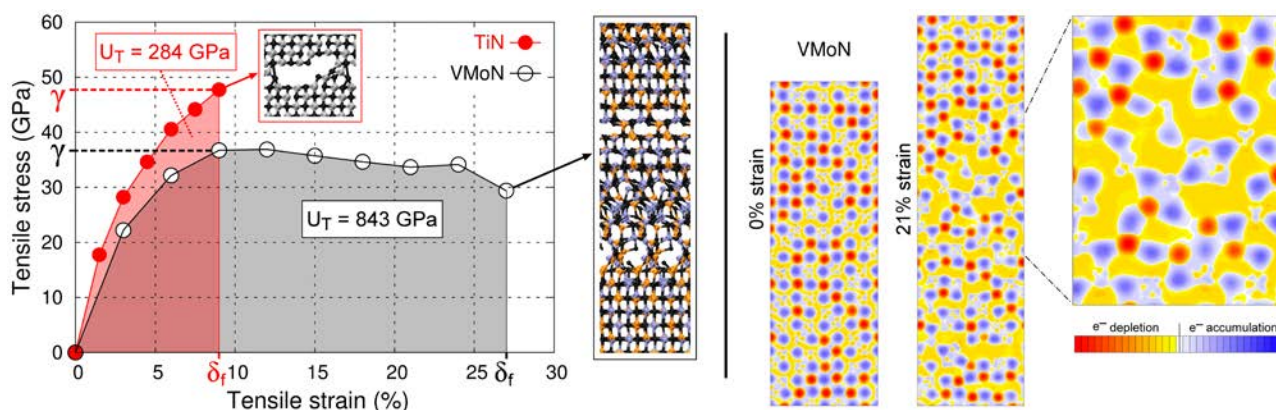
Inherent toughness and fracture mechanisms of refractory transition-metal nitrides via density-functional molecular dynamics

D.G. Sangiovanni^{1,2}

¹Atomistic Modelling and Simulation, ICAMS,
Ruhr-Universität Bochum, D-44801 Bochum, Germany

²Department of Physics, Chemistry, and Biology (IFM),
Linköping University, SE-58183 Linköping, Sweden

Hard refractory transition-metal nitrides possess unique combinations of outstanding mechanical and physical properties, but are typically brittle. Recent experimental results demonstrated that single-crystal NaCl-structure (B1) $V_{0.5}Mo_{0.5}N$ pseudobinary solid solutions are both hard (~20 GPa) and ductile; that is, they exhibit toughness, which is unusual for ceramics. However, key atomic-scale mechanisms underlying this inherent toughness are unknown. Here, I carry out density-functional *ab initio* molecular dynamics (AIMD) simulations at room temperature to identify atomistic processes and associated changes in the electronic structure which control strength, plasticity, and fracture in $V_{0.5}Mo_{0.5}N$, as well as reference B1 TiN, subject to $\langle 001 \rangle$ and $\langle 110 \rangle$ tensile deformation. AIMD simulations reveal that $V_{0.5}Mo_{0.5}N$ is considerably tougher than TiN owing to its ability to (i) isotropically redistribute mechanical stresses within the elastic regime, (ii) dissipate the accumulated strain energy by activating local structural transformations beyond the yield point. In direct contrast, TiN breaks in brittle manner when applied stresses reach its tensile strength. Charge transfer maps show that the adaptive mechanical response of $V_{0.5}Mo_{0.5}N$ originates from highly populated *d-d* metallic-states, which allow for counterbalancing the destabilization induced via tensile deformation by enabling formation of new chemical bonds. The high ionic character and electron-localization in TiN precludes the possibility of modifying bonding geometries to accommodate the accumulated stresses, thus suddenly causing material's fracture for relatively low strain values.



Keywords: Refractory transition-metal nitrides; Ab initio molecular dynamics; Toughness; Fracture; Electronic structures

Dr. Davide G. Sangiovanni: davide.sangiovanni@ruhr-uni-bochum.de, davsan@ifm.liu.se

1. Introduction

Refractory transition-metal (TM) nitrides, a class of technologically important materials characterized by unique combinations of properties [1-5], are widely employed as protective coatings for industrial machining [6, 7], diffusion-barrier layers in electronic devices [8-12], and biocompatible coatings [13-15]. More recently, it has also been shown that these materials are promising candidates for applications in catalysis [16], energy storage and conversion [17, 18], and plasmonics [19]. As most ceramics, however, TM nitrides are generally brittle: thermally- or mechanically-induced stresses rapidly lead to fracture, thus limiting their potential use. Toughness in TM nitrides is typically enhanced in extrinsic manner, e.g., by nanoengineering superlattice or nanocomposite structures, which block or deflect propagating cracks at grain boundaries or interfaces to prevent brittle failure [20-22]. Recent experiments [23, 24], motivated by *ab initio* theoretical predictions [25], demonstrated that single-crystal NaCl-structure (B1) $V_{0.5}Mo_{0.5}N$ solid solutions (denoted below as VMoN) are inherently *both* hard and ductile (i.e. tough). This surprising finding addressed a long-standing question in materials science on whether high hardness/strength and good ductility/plasticity are necessarily mutually exclusive properties in a single-crystal ceramic phase.

Density-functional theory (DFT) investigations have indicated that the intrinsic ductility of VMoN, as well as of nearly isoelectronic TM nitride solid solutions, is primarily an effect of optimized occupation of bonding metallic *d-d* states near the Fermi energy, which renders the material more compliant to shearing [25-27]. Recently, it has also been suggested that metastable B1 TM nitride alloys formed upon mixing cubic and hexagonal binary phases possess enhanced ductility due to energetically-favored formation of stacking faults that allows for dissipating accumulated stresses during $\{111\}\langle 1\bar{1}0\rangle$ slip [28]. However, previous theoretical investigations were carried out at 0 Kelvin. The explicit inclusion of temperature in *ab initio* modeling is necessary to reveal atomistic processes with associated changes in electronic structures that govern the ductile vs. brittle mechanical behavior of single-crystal TM nitrides.

In this work, I carry out density-functional *ab initio* molecular dynamics (AIMD) simulations to clarify the synergistic effects of lattice vibrations and electronic structures on the onset of plastic

deformation, as well as of crack formation in bulk $V_{0.5}Mo_{0.5}N$ and TiN (here considered as reference hard but brittle nitride system [23]) subject to tensile strain. I identify atomistic pathways leading to materials' structural transformation and fracture, thus providing novel insights into the modalities by which mechanical yielding, plastic deformation, and bond rupture take place in intrinsically brittle (TiN) vs. inherently ductile (VMoN) transition metal nitride ceramics.

2. Computational details and methods

Density-functional *ab initio* molecular dynamics (AIMD) [29] simulations are carried out using the VASP code [30] implemented with the projector augmented wave method [31]. The electronic exchange and correlation effects are treated with the Armiento-Mattsson approximation [32]. The Newton's equations of motion are integrated at 1-fs timesteps by sampling the *NVT* canonical phase space. At each time-step, the total energy is evaluated to an accuracy of 10^{-5} eV/atom, employing Γ -point sampling of the Brillouin-zone and a plane-wave cutoff energy of 300 eV.

AIMD tensile-deformation testing is performed by sequentially elongating [001]- and [110]-oriented defect-free cubic-B1 TiN and $V_{0.5}Mo_{0.5}N$ supercell boxes [denoted below as TMN(001) and TMN(110)] along their vertical axis (z) at strain steps of 1.5%, while maintaining unvaried lateral supercell sizes. All simulation supercells are formed of 24 atomic layers for a total of 192 nitrogen and 192 metal atoms, applying periodic boundary conditions in x , y , and z directions. The relationship between simulation-box vs. crystallographic in-plane directions are $x = [\bar{1}10]$ and $y = [110]$ for structures of vertical [001]-orientation, whereas $x = [1\bar{1}0]$ and $y = [001]$ for [110]-oriented supercells. Short- and long-range CuPt-like 111 cation ordering has been observed in B1 $V_{0.5}W_{0.5}N$ [33] and rhombohedral (111-distortion of the B1 structure) $Ti_{0.5}W_{0.5}N$ [34] solid solutions. On the contrary, lattice ordering has not been reported for B1 $V_{0.5}Mo_{0.5}N$ samples [23, 24, 35, 36]. Thus, the special quasirandom structure approach [37] is used to minimize the degree of short-range ordering on the $V_{0.5}Mo_{0.5}N$ cation sublattice. At each strain step, the supercells are first (*i*) rapidly equilibrated at 300 K via an isokinetic thermostat (velocity rescaling for 300 time steps) to efficiently dissipate

the excess energy caused by volume changes, then (ii) maintained at room temperature for additional 2.7 ps using the Nosé-Hoover thermostat. The model systems are elongated up to materials' fracture. Fracture, identified in AIMD runs as abrupt variations in atomic velocities and stresses, is characterized by a rapid sequence of bond snapping. AIMD videos are created with the software Visual Molecular Dynamics [38] and can be found in the supplemental material [39]. The normal and shear stresses induced in the materials by tensile deformation are directly extracted from VASP output. Integration of the area underlying vertical-stress (σ_z) vs. strain curves allows evaluating the ideal tensile toughness of defect-free B1 TiN and B1 $V_{0.5}Mo_{0.5}N$ ceramics.

The use of defect-free bulk structures provides qualitative comparisons between the ideal resistances to fracture in different TM nitrides; a fundamental step for subsequent investigations of the mechanical behavior in defective structures. Below, the following notations are used: tensile toughness = U_T , moduli of resilience = U_r , strain along [h k l] crystallographic direction = $\delta^{[h\ k\ l]}$, elongation at fracture points = δ_f , yield strengths = γ , and stress components: lateral (σ_x and σ_y), vertical (σ_z), and shearing (σ_{xy} , σ_{yz} , and σ_{xz}) stresses. All stresses are given in absolute values. Bond-angle analyses, based on the approach described in Ref. [40], are used to identify the changes in local atomic coordination induced by tensile strain. The percentage of fcc, bcc, and hcp local atomic environments are calculated at each timestep by using the software Ovito [41]. The percentages are separately determined for the anion and cation sublattices, and then averaged. The bond-angle analysis is performed on fractional atomic coordinates in order to eliminate the effects of uniaxial supercell stretching on local lattice symmetries.

Electron transfer maps, determined via DFT for lattice configurations extracted directly from AIMD trajectories, are obtained by subtracting the superposition of non-interacting atomic electron densities from self-consistent charge densities. For these calculations, the Brillouin zone is integrated on $3 \times 3 \times 3$ k-point grids while the cutoff energy is set to 400 eV.

3. Results and discussion

Ductility, materials' ability to deform plastically, can be assessed as the elongation at the fracture point (δ_f) during tensile deformation. Good ductility combined with high mechanical strength (γ) equates to high toughness, a measure of the energy (per unit volume) required to deform a material up to rupture.

Materials' toughness corresponds to the area underlying tensile stress σ_z vs. strain curves. Fig. 1a illustrates stress/strain curves obtained by applying [001] deformation to TiN(001) and VMoN(001) structures. The results demonstrate that the pseudobinary alloy is considerably tougher than the binary nitride phase ($U_T^{\text{VMoN}(001)} = 843$ GPa vs. $U_T^{\text{TiN}(001)} = 284$ GPa). The plot in Fig. 1b confirms that VMoN is tougher than TiN also with respect to [110] tensile strain ($U_T^{\text{VMoN}(110)} = 608$ GPa vs. $U_T^{\text{TiN}(110)} = 515$ GPa). The present theoretical findings are consistent with previous fracture toughness experiments which evidence opposite mechanical behaviors for single-crystal B1 TiN vs. VMoN: TiN samples crack in all nanoindentation tests while VMoN films dissipate the internal stresses by plastic flow leading to material pile-up adjacent to the indented area [23].

TiN(001) subject to [001] tensile strain maintains octahedral NaCl-type coordination up to fracture. Fig. 2 illustrates a sequence of AIMD snapshots of TiN(001) strained up to its maximum [001]-elongation (9%). At this strain, AIMD videos show frequent Ti–N bond snapping events, which cause continuous changes in bonding configurations and formation of voids. During 1.9 ps, the voids grow until TiN cracks forming two surfaces orthogonal to the applied strain. Mechanical failure occurs via cleavage of (001) planes.

Analogous to the behavior described for TiN(001), also TiN(110) cracks in brittle manner, with atoms maintaining rocksalt-like octahedral coordination up to structural failure. Nevertheless, TiN(110) supercells sustain extensions up to 13.5% (Fig. 3), that is, superior to the strain at fracture of TiN(001). Moreover, bond snapping in TiN(110) is initiated relatively more slowly than in TiN(001). The material withstands the stress (all Ti–N bonds remaining intact) at maximum elongation during two ps. However, AIMD videos show a progressive increase in lattice vibrational amplitudes along the [110] direction which, after 2 ps, lead to a rapid concatenation of bond breakage

and ultimately cause material's brittle failure. The nearest-neighbor bonds in unbroken lattice regions (indicated by square red brackets in Fig. 3) elastically recover their optimal 90° angles after fracture. This demonstrates that single-crystal B1 TiN cracks because unable to dissipate the elastic energy accumulated during tensile deformation.

TiN does not undergo any structural transformation during both [001] or [110] tensile strain. Thus, within the defect-free model considered in this work, the TiN mechanical response to uniaxial deformation exhibits elastic behavior up to brittle failure. This also implies that the values of external pressures at maximum TiN elongation are good estimates of TiN yield strengths ($\gamma^{\text{TiN}(001)} \approx 48$ GPa for $\delta_f^{\text{TiN}(001)} = 0.090$ and $\gamma^{\text{TiN}(110)} \approx 53$ GPa for $\delta_f^{\text{TiN}(110)} = 0.135$) and that moduli of resilience U_r account for the total toughness U_T of the material ($U_r^{\text{TiN}(001)} = 284$ GPa and $U_r^{\text{TiN}(110)} = 515$ GPa), see Fig. 1. It should be noted that mechanical strength values calculated for defect-free crystals (of the order of tens of GPa in the case of TM nitrides and carbides [42]) are ideal upper bounds – often largely exceeding experimentally-determined values – for the strength attainable in real systems.

Unstrained B1 $V_{0.5}Mo_{0.5}N$ supercells exhibit buckled bonding geometries at room temperature (see Fig. 4a). This is due to strongly anharmonic energy landscapes – also characteristic of rocksalt Group-VB mononitrides – with potential energy minima offset from ideal B1 lattice sites (see figure 5 in [43] and figure 1 in [44]) which cause dynamical instability of the cubic binary phases at 0 Kelvin [45]. In the case of VN, the formation of V_4 tetrahedral clusters [46] at temperatures lower than ≈ 250 K reduces the lattice symmetry from B1 to tetragonal [47]. At room temperature, the thermal energy is sufficient [48] to enable diffusionless tetragonal \rightarrow B1 lattice transformations via randomization (shuffling) of atomic displacements along $\langle 111 \rangle$ B1 crystallographic directions [49]. This stabilizes the rocksalt structure both dynamically and thermodynamically owing to a significant contribution of the vibrational entropy to the Gibbs free energy [47]. Analogous to VN, $V_{0.5}Mo_{0.5}N$ random solid solutions also exhibit clustering of metal atoms due to strong $d-d$ orbital constructive interactions (note, for example, electron accumulation between metal/metal pairs in SQS VMoN in figure 4e of Ref. [27]). In the case of $V_{0.5}Mo_{0.5}N$, however, the shuffling of atomic displacements

around B1 positions at finite-temperatures is further promoted by the lattice configurational disorder. This is important because it allows the ternary alloy to distribute stresses in an isotropic manner, thus alleviating the burden caused by uniaxial deformation (see below).

AIMD simulations reveal that VMoN alloys subject to tensile deformation undergo several structural changes that prevent brittle fracture. For relatively small tensile deformations ($< 12\%$), metal and N atoms in VMoN(001) primarily maintain their octahedral coordination as in the unstrained B1 structure (see Fig. 4a). For $\delta^{[001]} > 12\%$, however, a significant portion of the lattice becomes much less densely packed in comparison with the unstrained crystal. Fig. 4b illustrates VMoN(001) elongated by 21%. The high stresses induce local bending of several metal–N bonds, with bond angles which increase from $\approx 90^\circ$ to $120\text{--}140^\circ$, causing a decrease from 6 to 4 – 5 (more details below) in the average atomic coordination number (see lattice portion indicated by a red square bracket in Fig. 4b). Although already considerably deformed, VMoN(001) sustains an additional 6% tensile strain before breakage (Fig. 4c). This evidences the fact that the cage-like structure itself (marked with red square brackets in Fig. 4b and 4c) is highly mechanically resistant. The maximum tensile strain reached by VMoN(001) in AIMD simulations, $\square\delta_f^{\text{VMoN}(001)} = 0.270$, is three times greater than the value, $\square\delta_f^{\text{TiN}(001)} = 0.090$, determined for TiN(001) (see Fig. 1a).

Consistent with the results described above for VMoN(100) systems, AIMD simulations of VMoN(110) subject to $[110]$ tensile strain confirm the excellent ability of the ternary alloy structure to withstand elongation by undergoing several local transformations. In addition, the results obtained for $[110]$ -oriented supercells facilitate the understanding of other important aspects regarding the inherent toughness and plasticity of B1 VMoN crystals.

Fig. 5a illustrates a series of AIMD snapshots taken for VMoN(110) strained along $[110]$ by 6, 12, 13.5, 15, 16.5, and 18%. The sixfold octahedral atomic coordination is fully preserved up to strains of $\approx 6\%$. For vertical $[110]$ elongations increasing from 6 to 12%, AIMD videos show a progressive bond strengthening between V–V and, to a lower extent, V–Mo pairs along the $[1\bar{1}0]$ direction (i.e., normal to the applied tensile deformation). The effect can be seen in the magnification

of 12%-strained structures in the lower left panel of Fig. 5a and is indicated by blue-color horizontal V–V bonds. The considerable reinforcement of lateral metal/metal interactions observed in 12%-extended lattices is demonstrated by the fact that the bond lengths ($\leq 2.4 \text{ \AA}$) in metal/metal pairs formed during deformation are approximately 20% shorter than the average metal/metal interatomic spacing ($\approx 3 \text{ \AA}$) in unstrained VMoN.

Due to configurational disorder on the cation sublattice, the distribution of shortened/stretched $[\bar{1}10]$ -oriented metal/metal bonds is not homogeneous throughout the material. Domains characterized by higher concentrations of V atoms exhibit the largest density of metal/metal pairs with strengthened bonds (primarily V–V pairs). The fact that V–V pairs form more frequently than V–Mo or Mo–Mo pairs is likely due to the vibrational amplitudes of V atoms being larger than those of heavier Mo atoms. The formation of metal/metal pairs produces $[\bar{1}10]$ normal stresses σ_x orthogonal to the applied tensile deformation. Moreover, the random spatial arrangement of metal pairs induces a modulation in strain fields, which varies among different (110) lattice layers depending on the local density of shortened/stretched interatomic bonds. The inhomogeneity of internal strains generates shear stresses (σ_{xz}) that cause bond bending within (001) crystallographic planes. The effect is indicated with a red dashed line in the bottom-left panel of Fig. 5a.

Fig. 5c shows that the intensity of σ_x , as well as of σ_{xz} stresses increases with the vertical elongation of VMoN(110) crystals up to $\square\delta^{[001]} = 0.09$. For $\delta^{[001]} > 0.09$, the σ_{xz} shear stress is sufficiently strong to twist the bonding network, thus causing local partial rotations of (001) atomic layers about the [001] crystallographic axis, similar to nucleation of a disclination (see schematic clarification in Fig. 5b). The green solid ellipse in the lower-left panel ($\delta^{[110]} = 0.12$) of Fig. 5a shows a VMoN distorted lattice region after the rotation of different (001) lattice planes relative to each other. The mechanism of relative rotation of (001) lattice planes had been detected by selected-area electron diffraction patterns acquired for plastically-deformed regions of B1 $V_{0.5}Mo_{0.5}N$ films (see figure 6 in Ref. [24]).

For vertical tensile strains $\delta^{[110]} > 0.09$, VMoN(110) is able to partially dissipate σ_x and σ_{xz} stresses upon activating the relative rotation of lattice layers (Fig. 5c), as anticipated above. Both lateral σ_x and shearing σ_{xz} stress values remain approximately constant for $\delta^{[110]} > 0.12$. For tensile extensions $\delta^{[110]}$ greater than 0.12, the mechanical energy introduced in the system is continuously converted into small additional relative rotations of (001) lattice planes. This causes a significant distortion of the bonding network and changes in local atomic coordination, as illustrated in the lower-center panel of Fig. 5a for $\delta^{[110]} = 0.15$. Further torsions lead to interatomic-bond fraying. VMoN(110) fractures in ductile manner at a tensile strain of $\delta_f^{\text{VMoN}(110)} = 0.18$ (see lower-right panel in Fig. 5a). As a reference, TiN(110) cracks in brittle manner at a smaller relative elongation of 13.5%. The results obtained for [001] and [110] tensile deformation are consistent with the experimental observations, which demonstrated that VMoN pseudobinary alloys are considerably more ductile and tougher than the binary nitride [23, 24, 36].

The findings described so far clarify the dynamics of atomistic mechanisms that confer single-crystal B1 VMoN alloys with intrinsic ductility. However, experiments demonstrated that VMoN is not only ductile, but also very hard (≈ 20 GPa [23, 24]). Hardness, materials resistance to plastic deformation, is largely controlled by the mobility of dislocations. *Ab initio* calculations of dislocation core structures and energetics in ceramic materials, such as B1 MgO [50], are practically limited by the large supercell sizes required to embed the linear defect, and are thus beyond the scope of this work. Nevertheless, mechanical strength and hardness are generally well-correlated materials' properties [51, 52]. The plots presented in Fig. 1 show that single-crystal B1 VMoN and TiN possess similar ideal tensile strengths ($\gamma^{\text{VMoN}(001)} \approx 37$ GPa and $\gamma^{\text{VMoN}(110)} \approx 44$ GPa vs. $\gamma^{\text{TiN}(001)} \approx 48$ GPa and $\gamma^{\text{TiN}(110)} \approx 53$ GPa), in agreement with the fact that the two materials exhibit comparable hardness ($H^{\text{VMoN}} \approx 20$ GPa [23, 24] vs. $H^{\text{TiN}} \approx 18 - 23$ GPa [23, 53, 54]). The model employed here provides novel insights into atomic-scale processes responsible for the inherent mechanical strength and hardness of monolithic cubic VMoN and TiN crystals.

AIMD results suggest different mechanisms at the origin of the elevated strength/hardness in

VMoN vs. TiN. The simulations reveal that VMoN alloys subject to tensile strain are able to distribute internal stresses in an isotropic manner. Lateral σ_x and σ_y , and vertical (i.e. parallel to the tensile deformation) σ_z stresses are nearly equivalent up to material fracture (see Fig. 6a and 6b). This phenomenon may explain the high hardness measured for B1 VMoN single-crystals [23, 24]. During nanoindentation testing, the load applied by the tip is partially stored in elastic strain-energy and partially dissipated via plastic deformation. VMoN partitions the accumulated strain energy in bonds both orthogonal and parallel to the tensile strain, thus alleviating the burden produced by deformation on individual bonds. For external loads confined to the elastic-response regime, the material recovers (to a large extent) its original structure, thus resulting in elevated hardness. In contrast, high strength and hardness in TiN derive primarily from uniaxial resistance to deformation, as evidenced by the fact that σ_z stress values show a much steeper increase with strain in comparison with lateral stresses σ_x and σ_y (Fig. 6c and 6d). The much higher directionality in mechanical response to stresses reflects the fact that TiN exhibits larger uniaxial and shear elastic constants [$C_{11} = 640$ GPa and $C_{44} = 159$ GPa [27]], as well as a lower elastic constant $C_{12} = 115$ GPa, Poisson's ratio $\nu \approx 0.3$, and anisotropy factor $A \approx 0.6$ [27] than SQS VMoN [$C_{11} = 465$ GPa, $C_{44} = 90$ GPa, $C_{12} = 212$ GPa, $\nu \approx 0.4$, and $A \approx 0.7$ [27]]. Hence, TiN mechanical failure occurs at the material yield point via cleavage of lattice planes because the highly anisotropic distribution of stresses produces an overloading on bonds parallel to the strain direction.

The transformations observed within plastically-deformed domains of VMoN(001) and VMoN(110) are associated with a progressive alteration of the potential energy landscape and chemical environment surrounding the nuclei. Local changes in lattice symmetry can be quantified via bond-angle (see Sec. 2) and average coordination-number analyses. The results illustrated in Fig. 7 demonstrate the ability of VMoN to gradually modify its structure in order to accommodate external stresses and prevent fracture.

For both (001)- and (110)-oriented supercells (Fig. 7a and 7b), the percentage in local lattice symmetry progressively changes from pure fcc (unstrained VMoN) to 40% fcc + $\approx 10\%$ bcc + $\approx 10\%$

hcp + other configurations (VMoN at fracture point). The reduction in lattice symmetry presents an approximately quadratic dependence on strain, with atomic environments that essentially remain B1-like from 0 up to ~9% supercell elongation. This is also reflected by the variation in first-neighbor atomic-coordination. For both VMoN(001) and VMoN(110), the average coordination number, calculated over the entire supercell, decreases from 6 to ~5.4 (filled black dots in the insets of Fig. 7a and 7b). However, as illustrated by cyan filled dots in the insets of Fig. 7a and 7b, the average coordination number within strongly-modified VMoN regions slowly decreases from 5 (for $\delta^{[001]}$ and $\delta^{[110]} \approx 10\%$) to ~4.5 (at fracture points). In direct contrast, TiN maintains octahedral fcc-like coordination, while subject to uniaxial strain: the coordination number remains approximately equal to 6 up to fracture (black dots in the insets of Fig. 7c and 7d). The material undergoes a sudden mechanical failure at its yield point (see drop in percentage of fcc symmetry, Fig. 7c and 7d). The average coordination number of atoms at cleaved TiN surfaces (cyan dots in the insets of Fig. 7c and 7d) is ~4.5.

The results of this work evidence the remarkable selective mechanical behavior of VMoN ceramics. Within the elastic regime, the alloy responds in a hard manner to external solicitations owing to its ability to isotropically distribute stresses. However, when external loads approach or overcome the material's yield strength, VMoN activates local structural transformations that allow dissipation of accumulated stress. Electron-density analyses of tensile-deformed structures obtained during AIMD simulations demonstrate that the outstanding inherent toughness of VMoN solid solutions originates from high valence electron concentration (VEC = 10.5 e^- per formula unit) and high metallic character. These enable electron reorganization and formation of new bonds which energetically counterbalances the destabilization caused by deformation, as also suggested by DFT results at 0 Kelvin [25, 26].

DFT electron transfer maps show that the chemical bonds in TiN remain primarily ionic during elongation, as indicated by spherical charge distributions centered at the nuclei positions in unstrained vs. 7.5%-strained TiN(001) (Fig. 8). The localization of electrons near nuclear sites limits

the material's ability to form new bonds during deformation and favors crack nucleation and propagation. Analogous observations would be made by plotting TiN charge densities on crystallographic planes other than the one shown in Fig. 8.

The effects induced on VMoN(001) electron reorganization by [001] deformation are conveniently visualized by different cross-sectional views parallel to the strain direction: $(1\bar{1}0)$ plane in Fig. 8 and (100) plane in Fig. 9. Both plots illustrate electron transfer in unstrained and 21%-strained VMoN(001). Opposite to TiN behavior, in pseudobinary VMoN solid solutions, some of the electrons gradually transfer from bonds parallel (metal/N) to bonds normal to the deformation (primarily metal/metal in Fig. 8 and metal/N in Fig. 9), thus allowing for storing the strain energy (high hardness) while internally redistributing stresses (resistance to breakage) within the elastic regime. However, when the external load exceeds the VMoN yield strength, electrons delocalize also along other crystallographic directions in order to enable structural transformations and allow the alloy to reach a much greater elongation without breaking.

4. Conclusions

Density-functional *ab initio* molecular dynamics (AIMD) simulations at room temperature are used to identify atomistic processes and associated changes in the electronic structure which control strength, plasticity, and rupture in B1 $V_{0.5}Mo_{0.5}N$, as well as reference brittle B1 TiN binaries, subject to $\langle 001 \rangle$ and $\langle 110 \rangle$ tensile deformation. AIMD simulations reveal that $V_{0.5}Mo_{0.5}N$ is considerably tougher than TiN owing to its ability to:

- Elastic regime: Store the elastic energy induced by the deformation via isotropic stress-redistribution, thus preventing brittle fracture while conferring high strength/hardness;
- Near/beyond yield point: Dissipate the accumulated strain energy by activating local structural transformations that significantly improve ductility.

The adaptive hard/ductile mechanical response of cubic $V_{0.5}Mo_{0.5}N$ pseudobinary alloys stems from highly populated $d-d$ electronic states that enhance metallic-like behavior without affecting the high strength characteristic of ceramics. Facile electron-transfer enables bond strengthening, that counterbalances the destabilization induced by tensile deformation, as well as modifications in the lattice structure to comply with excessive loads. In contrast, TiN is unable to redistribute stresses and activate structural transformations due to interatomic bonds remaining primarily ionic up to fracture. The stresses accumulate along the strain direction and lead, at the yield point, to sudden bond snapping and brittle failure via cleavage of lattice planes.

Acknowledgements

This research was carried out using resources provided by the Swedish National Infrastructure for Computing (SNIC), on the Gamma and Triolith Clusters located at the National Supercomputer Centre (NSC) in Linköping, on the Beskow cluster located at the Center for High Performance Computing (PDC) in Stockholm, and on the Kebnekaise cluster located at the High Performance Computing Center North (HPC2N) in Umeå, Sweden. I gratefully acknowledge financial support from the Olle Engkvist Foundation.

References

- [1] X.J. Chen, V.V. Struzhkin, Z.G. Wu, M. Somayazulu, J. Qian, S. Kung, A.N. Christensen, Y.S. Zhao, R.E. Cohen, H.K. Mao, R.J. Hemley, Hard superconducting nitrides, *Proceedings of the National Academy of Sciences of the United States of America* 102 (2005) 3198.
- [2] G. Abadias, M.B. Kanoun, S. Goumri-Said, L. Koutsokeras, S.N. Dub, P. Djemia, Electronic structure and mechanical properties of ternary ZrTa_nN alloys studied by ab initio calculations and thin-film growth experiments, *Physical Review B* 90 (2014) 144107.
- [3] L. Hultman, Thermal stability of nitride thin films, *Vacuum* 57 (2000) 1.
- [4] D. Gall, I. Petrov, J.E. Greene, Epitaxial Sc_{1-x}Ti_xN(001): Optical and electronic transport properties, *Journal of Applied Physics* 89 (2001) 401.
- [5] M. Mikula, D. Plašienka, T. Roch, K. Štyráková, L. Satrapinskyy, M. Drienovský, V. Girman, B. Grančič, A. Pleceník, P. Kúš, Structural evolution of TaN-alloyed Cr–Al–Y–N coatings, *Surface & Coatings Technology* 288 (2016) 203.

- [6] A. Hörling, L. Hultman, M. Oden, J. Sjölen, L. Karlsson, Mechanical properties and machining performance of Ti_{1-x}Al_xN-coated cutting tools, *Surface & Coatings Technology* 191 (2005) 384.
- [7] L. Ning, S.C. Veldhuis, K. Yamamoto, Investigation of wear behavior and chip formation for cutting tools with nano-multilayered TiAlCrN/NbN PVD coating, *International Journal of Machine Tools & Manufacture* 48 (2008) 656.
- [8] M. Mühlbacher, A.S. Bochkarev, F. Mendez-Martin, B. Sartory, L. Chitu, M.N. Popov, P. Puschnig, J. Spitaler, H. Ding, N. Schalk, J. Lu, L. Hultman, C. Mitterer, Cu diffusion in single-crystal and polycrystalline TiN barrier layers: A high-resolution experimental study supported by first-principles calculations, *Journal of Applied Physics* 118 (2015) 085307.
- [9] A.S. Bochkarev, M.N. Popov, V.I. Razumovskiy, J. Spitaler, P. Puschnig, Ab initio study of Cu impurity diffusion in bulk TiN, *Physical Review B* 94 (2016) 104303.
- [10] M.N. Popov, A.S. Bochkarev, V.I. Razumovskiy, P. Puschnig, J. Spitaler, Point defects at the $\Sigma 5$ (012)[100] grain boundary in TiN and the early stages of Cu diffusion: An ab initio study, *Acta Materialia* 144 (2018) 496.
- [11] J.S. Chun, I. Petrov, J.E. Greene, Dense fully 111-textured TiN diffusion barriers: Enhanced lifetime through microstructure control during layer growth, *Journal of Applied Physics* 86 (1999) 3633.
- [12] J.S. Chun, P. Desjardins, C. Lavoie, C.S. Shin, C. Cabral, I. Petrov, J.E. Greene, Interfacial reactions in epitaxial Al/TiN(111) model diffusion barriers: Formation of an impervious self-limited Wurtzite-structure AlN(0001) blocking layer, *Journal of Applied Physics* 89 (2001) 7841.
- [13] S. Pisanec, L.C. Ciacchi, E. Vesselli, G. Comelli, O. Sbaizero, S. Meriani, A. De Vita, Bioactivity of TiN-coated titanium implants, *Acta Materialia* 52 (2004) 1237.
- [14] B. Subramanian, C.V. Muraleedharan, R. Ananthakumar, M. Jayachandran, A comparative study of titanium nitride (TiN), titanium oxynitride (TiON) and titanium aluminum nitride (TiAlN), as surface coatings for bio implants, *Surface & Coatings Technology* 205 (2011) 5014.
- [15] N.C. Reger, V.K. Balla, M. Das, A.K. Bhargava, Wear and corrosion properties of in-situ grown zirconium nitride layers for implant applications, *Surface & Coatings Technology* 334 (2018) 357.
- [16] Y. Abghoui, A.L. Garden, V.F. Hlynsson, S. Bjorgvinsdottir, H. Olafsdottir, E. Skulason, Enabling electrochemical reduction of nitrogen to ammonia at ambient conditions through rational catalyst design, *Physical Chemistry Chemical Physics* 17 (2015) 4909.
- [17] J. Xie, Y. Xie, Transition Metal Nitrides for Electrocatalytic Energy Conversion: Opportunities and Challenges, *Chemistry - a European Journal* 22 (2016) 3588.
- [18] Y. Zhong, X. Xia, F. Shi, J. Zhan, J. Tu, H.J. Fan, Transition Metal Carbides and Nitrides in Energy Storage and Conversion, *Advanced Science* 3 (2016) 1500286.
- [19] P. Patsalas, N. Kalfagiannis, S. Kassavetis, Optical Properties and Plasmonic Performance of Titanium Nitride, *Materials* 8 (2015) 3128.
- [20] S.H. Zhang, E. Byon, M.X. Li, Y.Z. He, F. Cai, L. Wang, H.S. Li, S.H. Si, Realization of superhard nanocomposites with sufficient toughness: Superlattice nanocrystal-TiN/amorphous-(W,Ti)C-0.83 films, *Thin Solid Films* 519 (2011) 1901.
- [21] A.A. Voevodin, J.S. Zabinski, Supertough wear-resistant coatings with 'chameleon' surface adaptation, *Thin Solid Films* 370 (2000) 223.
- [22] M. Mikula, T. Roch, D. Plasienska, L. Satrapinskyy, P. Svec, Sr., D. Vlckova, M. Dvoranova, B. Grancic, M. Gregor, A. Plecenik, P. Kus, Thermal stability and structural evolution of quaternary Ti-Ta-B-N coatings, *Surface & Coatings Technology* 259 (2014) 698.

- [23] H. Kindlund, D.G. Sangiovanni, L. Martinez-de-Olcoz, J. Lu, J. Jensen, J. Birch, I. Petrov, J.E. Greene, V. Chirita, L. Hultman, Toughness enhancement in hard ceramic thin films by alloy design, *APL Materials* 1 (2013) 042104.
- [24] H. Kindlund, D.G. Sangiovanni, J. Lu, J. Jensen, V. Chirita, J. Birch, I. Petrov, J.E. Greene, L. Hultman, Vacancy-induced toughening in hard single-crystal $V_{0.5}Mo_{0.5}N_x/MgO(001)$ thin films, *Acta Materialia* 77 (2014) 394.
- [25] D.G. Sangiovanni, L. Hultman, V. Chirita, Supertoughening in B1 transition metal nitride alloys by increased valence electron concentration, *Acta Materialia* 59 (2011) 2121.
- [26] D.G. Sangiovanni, V. Chirita, L. Hultman, Electronic mechanism for toughness enhancement in $Ti_xM_{1-x}N$ (M=Mo and W), *Physical Review B* 81 (2010) 104107.
- [27] D. Edström, D.G. Sangiovanni, L. Hultman, V. Chirita, Effects of atomic ordering on the elastic properties of TiN- and VN-based ternary alloys, *Thin Solid Films* 571 (2014) 145.
- [28] D.G. Sangiovanni, L. Hultman, V. Chirita, I. Petrov, J.E. Greene, Effects of phase stability, lattice ordering, and electron density on plastic deformation in cubic TiWN pseudobinary transition-metal nitride alloys, *Acta Materialia* 103 (2016) 823.
- [29] R. Car, M. Parrinello, Unified approach for molecular dynamics and density-functional theory, *Physical Review Letters* 55 (1985) 2471.
- [30] G. Kresse, J. Hafner, Ab initio molecular dynamics for liquid metals, *Physical Review B* 47(1) (1993) 558.
- [31] P.E. Blöchl, Projector augmented-wave method, *Physical Review B* 50 (1994) 17953.
- [32] R. Armiento, A.E. Mattsson, Functional designed to include surface effects in self-consistent density functional theory, *Physical Review B* 72 (2005) 085108.
- [33] H. Kindlund, J. Lu, J. Jensen, I. Petrov, J.E. Greene, L. Hultman, Epitaxial $V_{0.6}W_{0.4}N/MgO(001)$: Evidence for ordering on the cation sublattice, *Journal of Vacuum Science & Technology A* 31 (2013) 040602.
- [34] F. Tian, J. D'Arcy-Gall, T.Y. Lee, M. Sardela, D. Gall, I. Petrov, J.E. Greene, Epitaxial $Ti_{1-x}W_xN$ alloys grown on $MgO(001)$ by ultrahigh vacuum reactive magnetron sputtering: Electronic properties and long-range cation ordering, *Journal of Vacuum Science & Technology A* 21 (2003) 140.
- [35] H. Kindlund, G. Greczynski, E. Broitman, L. Martínez-de-Olcoz, J. Lu, J. Jensen, I. Petrov, J.E. Greene, J. Birch, L. Hultman, $V_{0.5}Mo_{0.5}N_x/MgO(001)$: Composition, nanostructure, and mechanical properties as a function of film growth temperature, *Acta Materialia* 126 (2017) 194.
- [36] H. Kindlund, J. Lu, E. Broitman, I. Petrov, J.E. Greene, J. Birch, L. Hultman, Growth and mechanical properties of 111-oriented $V_{0.5}Mo_{0.5}N/Al_2O_3(0001)$ thin films (unpublished).
- [37] A. Zunger, S.H. Wei, L.G. Ferreira, J.E. Bernard, Special quasirandom structures, *Physical Review Letters* 65 (1990) 353.
- [38] W. Humphrey, A. Dalke, K. Schulten, VMD: Visual molecular dynamics, *Journal of Molecular Graphics & Modelling* 14 (1996) 33.
- [39] See supplemental material.
- [40] G.J. Ackland, A.P. Jones, Applications of local crystal structure measures in experiment and simulation, *Physical Review B* 73 (2006) 054104.
- [41] A. Stukowski, Visualization and analysis of atomistic simulation data with OVITO-the Open Visualization Tool, *Modelling and Simulation in Materials Science and Engineering* 18 (2010) 015012.
- [42] S.H. Jhi, S.G. Louie, M.L. Cohen, J.W. Morris, Mechanical instability and ideal shear strength of transition metal carbides and nitrides, *Physical Review Letters* 87 (2001) 075503.

- [43] P. Rehak, M. Cerny, D. Holec, Interface-induced electronic structure toughening of nitride superlattices, *Surface & Coatings Technology* 325 (2017) 410.
- [44] S. Hu, C. Xu, Y. Lao, Y. Wang, H. Zhang, G.-J. Zhang, J. Yang, The stabilization of the rocksalt structured tantalum nitride, *Journal of Applied Physics* 122 (2017) 045109.
- [45] E.I. Isaev, S.I. Simak, I.A. Abrikosov, R. Ahuja, Y.K. Vekilov, M.I. Katsnelson, A.I. Lichtenstein, B. Johansson, Phonon related properties of transition metals, their carbides, and nitrides: A first-principles study, *Journal of Applied Physics* 101 (2007) 123519.
- [46] F. Kubel, W. Lengauer, K. Yvon, K. Knorr, A. Junod, Structural phase transition at 205 K in stoichiometric Vanadium Nitride, *Physical Review B* 38 (1988) 12908.
- [47] A.B. Mei, O. Hellman, N. Wireklint, C.M. Schlepuetz, D.G. Sangiovanni, B. Alling, A. Rockett, L. Hultman, I. Petrov, J.E. Greene, Dynamic and structural stability of cubic vanadium nitride, *Physical Review B* 91 (2015) 054101.
- [48] The energy difference between the tetragonal and B1 VN phases (≈ 18 meV/atom) [see for example: V.I. Ivashchenko, P.E.A. Turchi, V.I. Shevchenko, E.I. Olifan, First-principles study of phase stability of stoichiometric vanadium nitrides, *Physical Review B* 84 (2011) 174108] is comparable to $k_B T$ (≈ 26 meV) at 300 K.
- [49] F. Kubel, H.D. Flack, K. Yvon, Electron densities in VN .1. High-precision X-ray diffraction determination of the valence-electron density distribution and atomic displacement parameters, *Physical Review B* 36 (1987) 1415.
- [50] Z.C. Wang, M. Saito, K.P. McKenna, Y. Ikuhara, Polymorphism of dislocation core structures at the atomic scale, *Nature Communications* 5 (2014) 3239.
- [51] M.A. Meyers, K.K. Chawla, *Mechanical Behavior of Materials*, Prentice Hall, Englewood Cliffs (1999).
- [52] G.E. Dieter, *Mechanical Metallurgy*, second edition, McGraw-Hill (1976).
- [53] C.S. Shin, D. Gall, N. Hellgren, J. Patscheider, I. Petrov, J.E. Greene, Vacancy hardening in single-crystal TiN_x(001) layers, *Journal of Applied Physics* 93 (2003) 6025.
- [54] H. Ljungcrantz, M. Oden, L. Hultman, J.E. Greene, J.E. Sundgren, Nanoindentation studies of single-crystal (001)-, (011)-, and (111)-oriented TiN layers on MgO, *Journal of Applied Physics* 80 (1996) 6725.

Figures

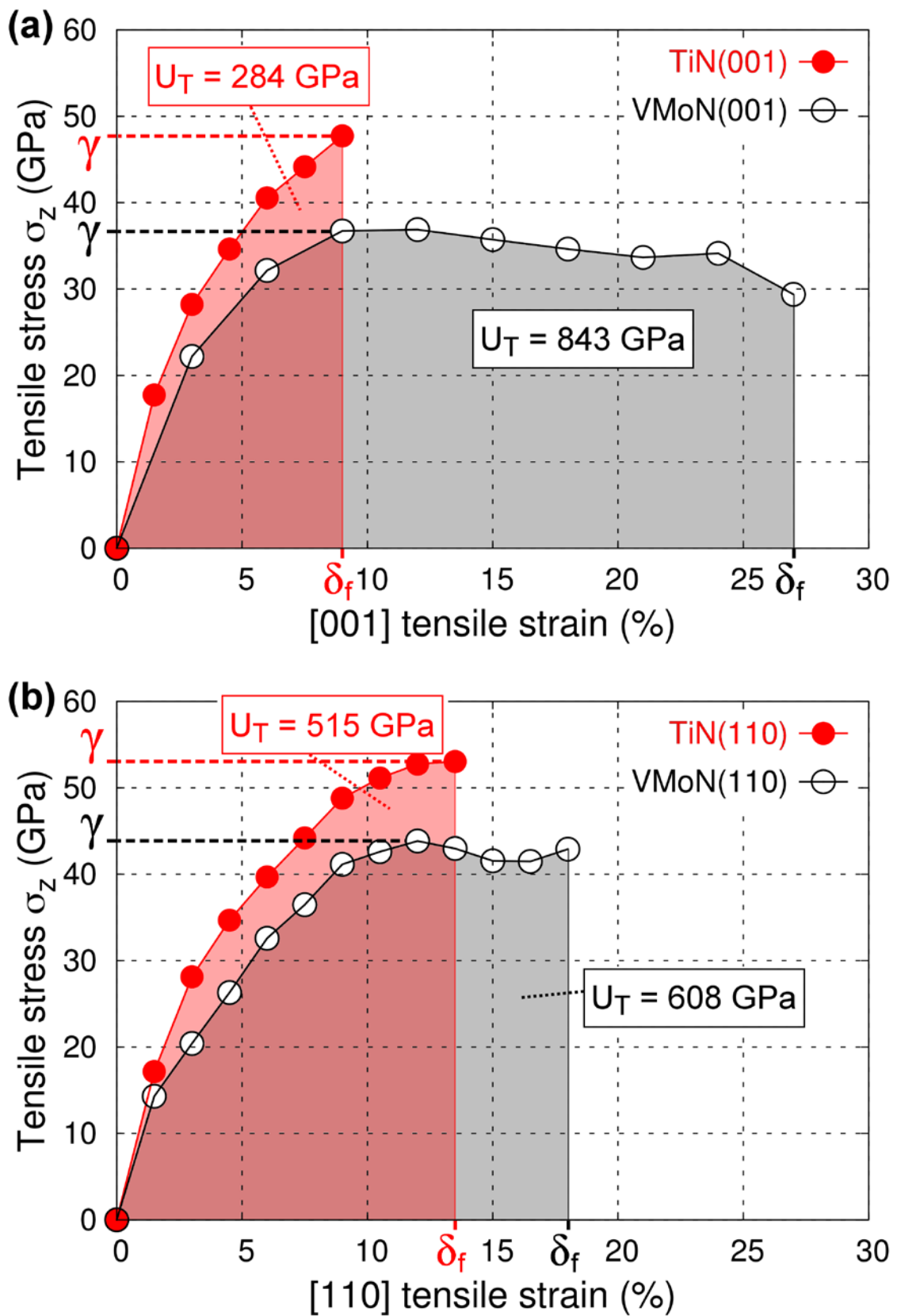


Fig. 1. Tensile stresses as a function of tensile strain obtained for (a) [001]-oriented and (b) [110]-oriented TiN and VMoN supercells during AIMD simulations at 300 K. U_T , γ , and δ_f indicate tensile toughness, yield strengths, and maximum elongations, respectively. Stresses are given in absolute values.

B1 TiN : 9% [001]-strain

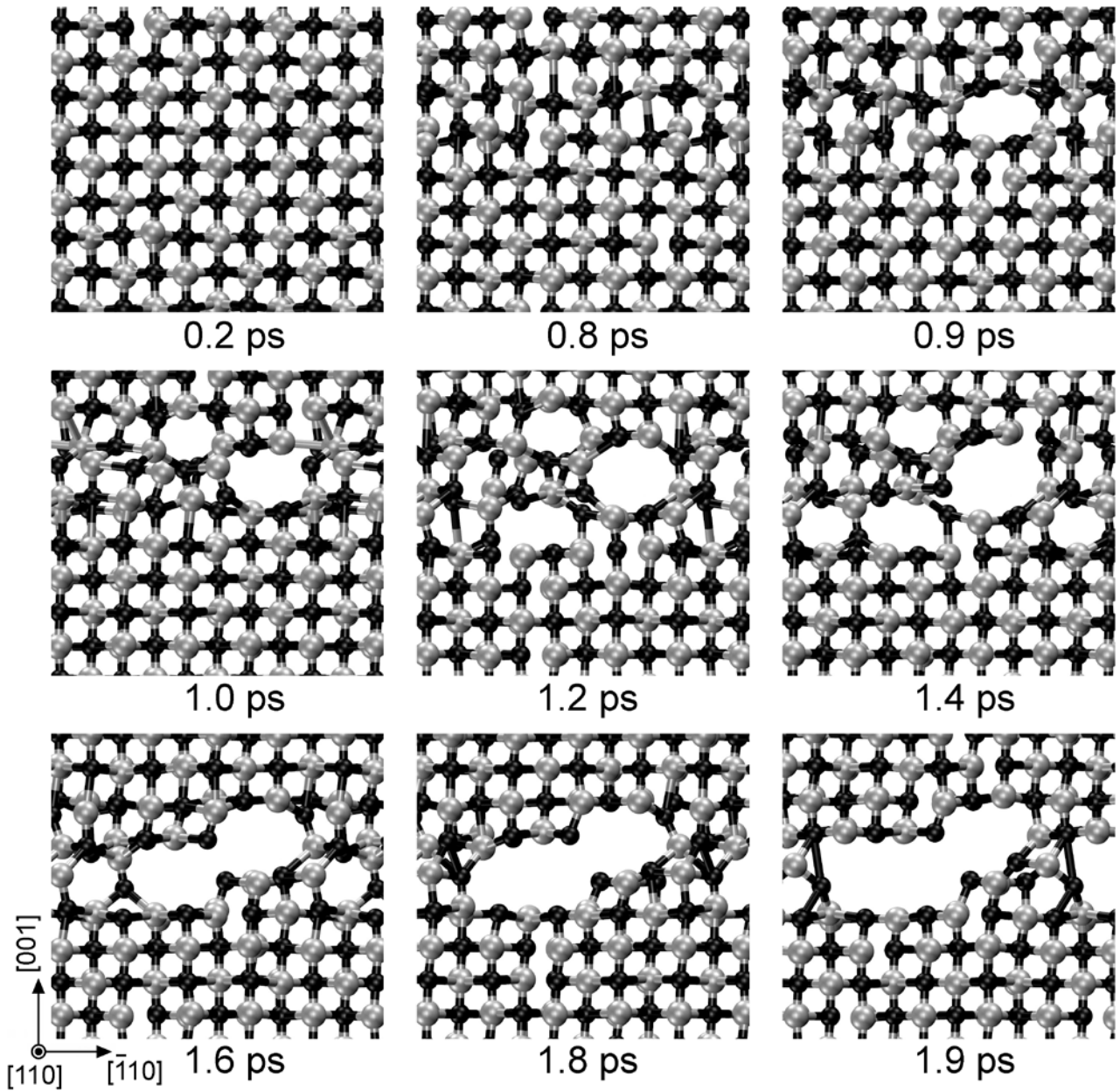


Fig. 2. AIMD snapshots of fracture dynamics in TiN(001) strained up to its maximum elongation (9%) at room temperature. The snapshots are taken at simulation times between 0.2 and 1.9 ps. The pictures' focus is on atoms surrounding the fractured region of the lattice. The cutoff length of bonds visualized in the figure is 2.6 Å. Ti (N) atoms are indicated by silver (black) spheres.

B1 TiN : 13.5% [110]-strain

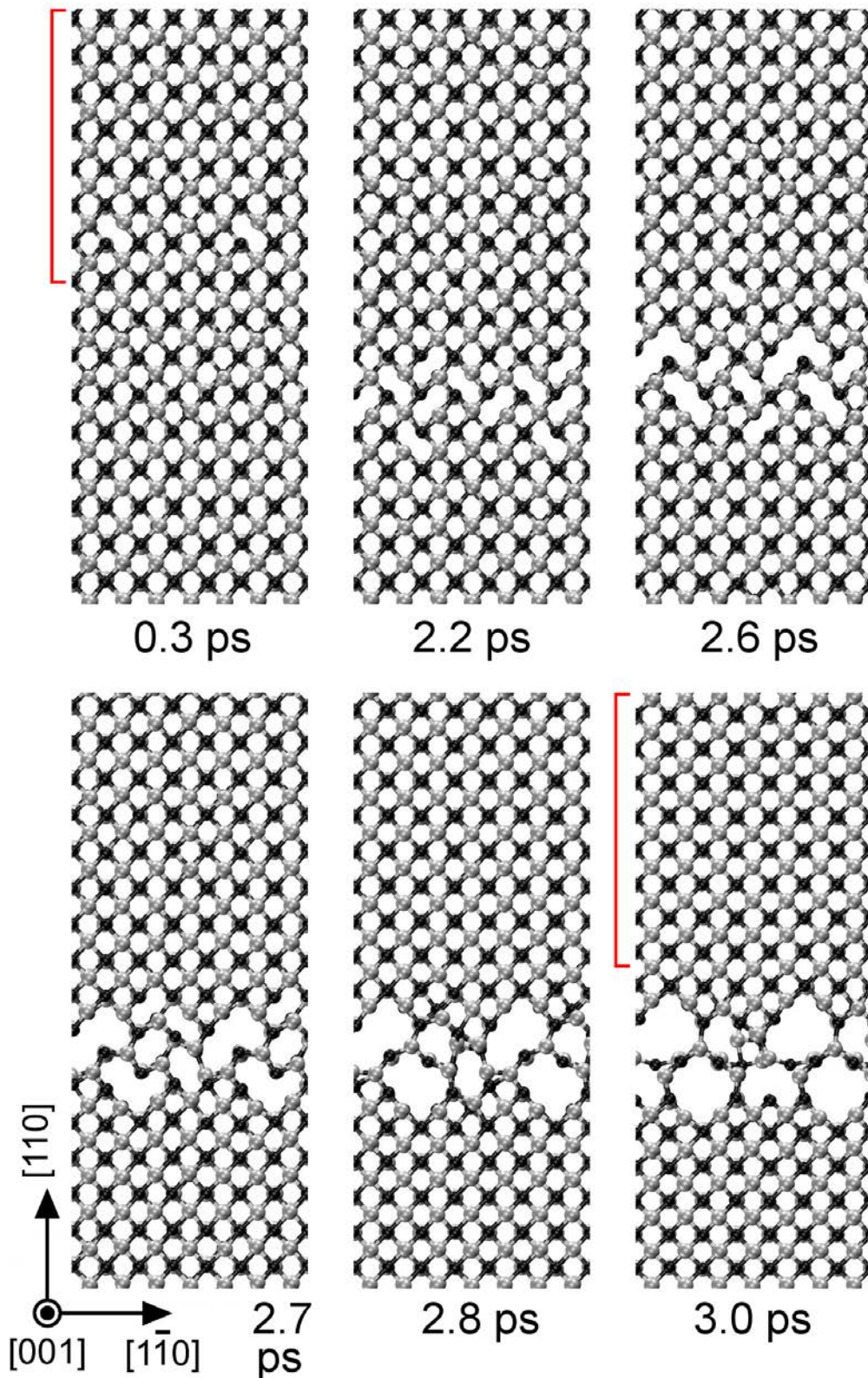


Fig. 3. AIMD snapshots of fracture dynamics in TiN(110) strained up to its maximum elongation (13.5%) at room temperature. The snapshots are taken at simulation times between 0.3 and 3.0 ps. The cutoff length of bonds visualized in the figure is 2.4 Å. The supercell regions enclosed by red square brackets [for 0.3 and 3.0 ps snapshots show the relaxation of bond angles to 90 degrees, and consequent shortening of (110) interlayer distances from ≈ 3.35 to ≈ 3 Å, after brittle failure at 3.0 ps. Ti (N) atoms are indicated by silver (black) spheres.

B1 $V_{0.5}Mo_{0.5}N$: [001]-strain

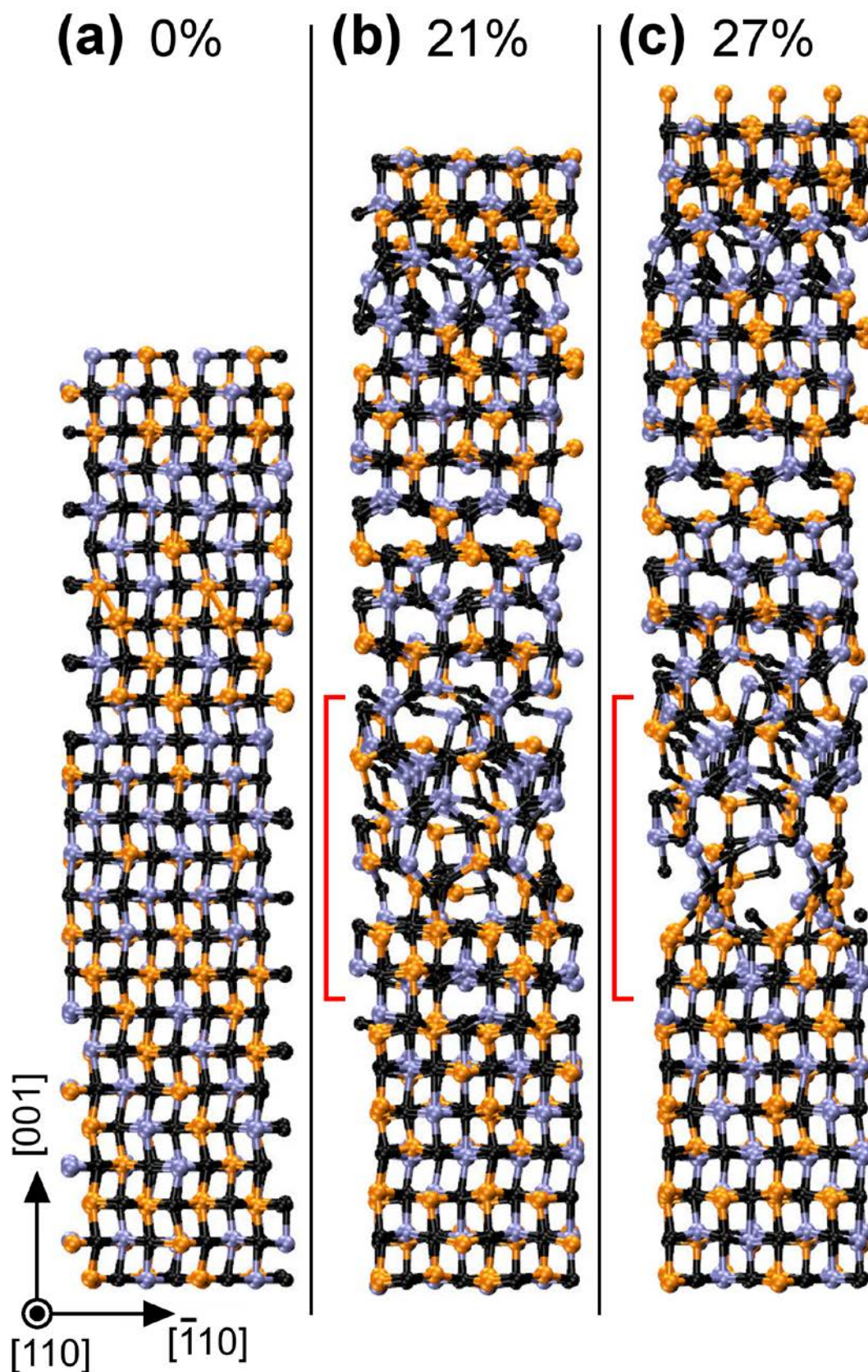


Fig. 4. Orthographic view of VMoN(001) supercells subject to [001] tensile deformation as determined via AIMD simulations at 300 K. The cutoff length of bonds visualized in the figure is 2.4 Å. N = black, Mo = orange, and V = blue spheres.

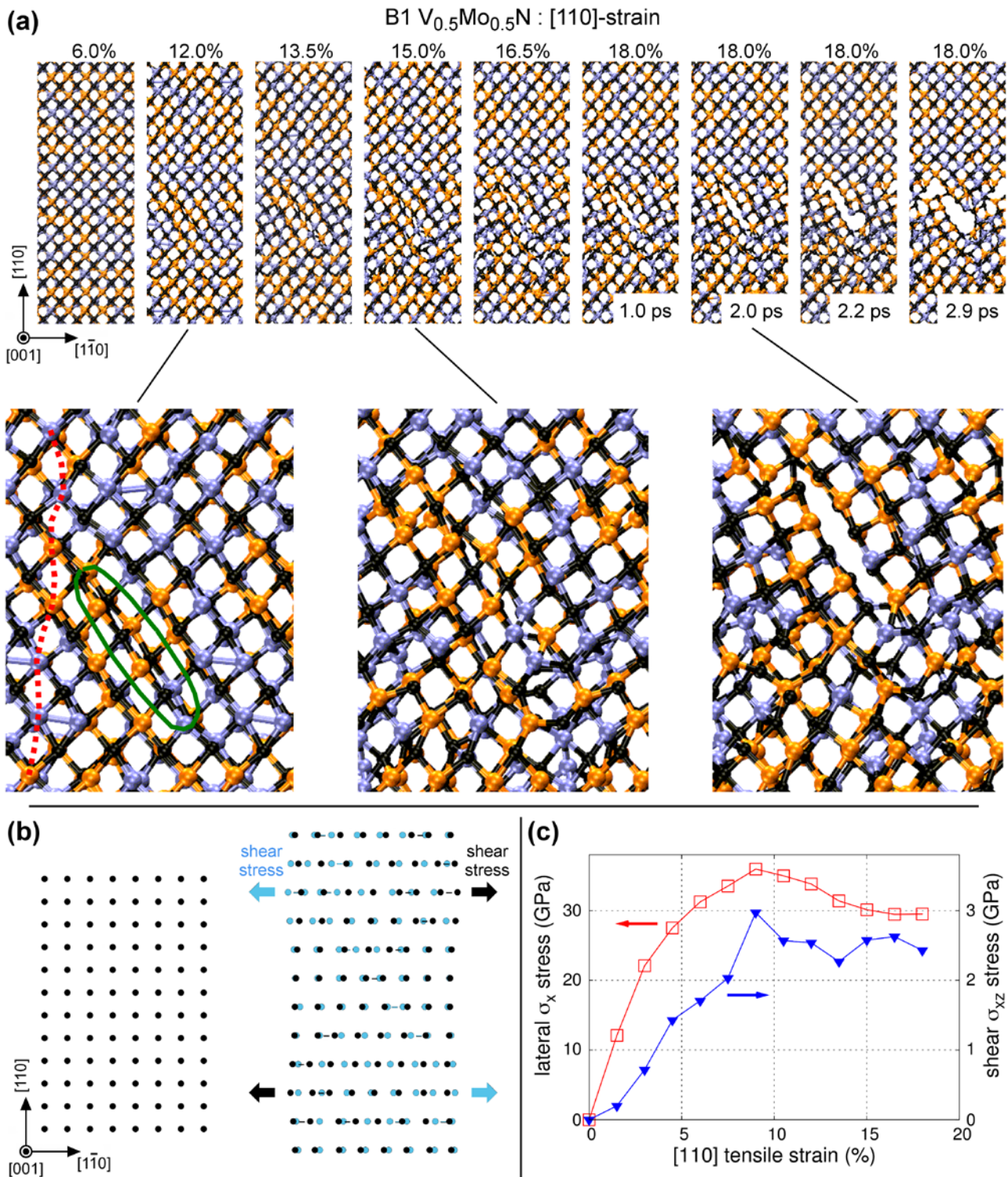


Fig. 5. (a) Orthographic view of VMoN(110) supercells subject to [110] tensile deformation (strains between 6 and 18%) as determined via AIMD simulations at 300 K. The cutoff length of bonds visualized in the figure is 2.4 Å. N = black, Mo = orange, and V = blue spheres. (b) Schematic representation of the generation of lateral σ_x and shear σ_{xz} stresses [associated with metal/metal bond strengthening within the (110) plane] induced by [110] tensile deformation. (c) Lateral σ_x (square symbols) and shear σ_{xz} (triangular symbols) stresses plotted as a function of vertical tensile strain, as determined during AIMD simulations. Stresses are given in absolute values.

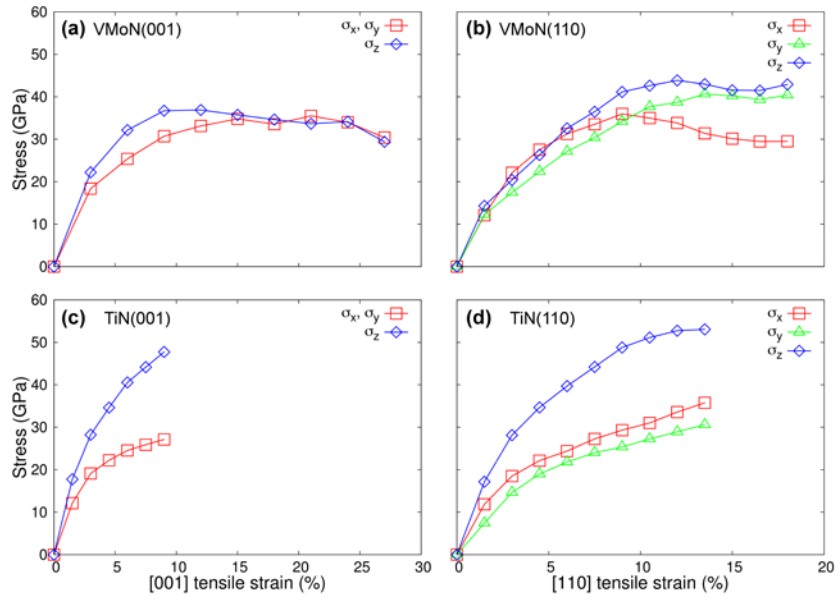


Fig. 6. Lateral σ_x and σ_y , and vertical σ_z stresses in VMoN and TiN subject to [001] and [110] (vertical supercell orientation) tensile deformation, as determined by averaging over stress values obtained for approximately 100 different AIMD configurations at each strain. For [001]-oriented supercells, the lateral directions x and y are equivalent by symmetry. Thus, the data represented by red solid curves in panels (a) and (c) are calculated as $(\sigma_x + \sigma_y)/2$. All stresses are given in absolute values.

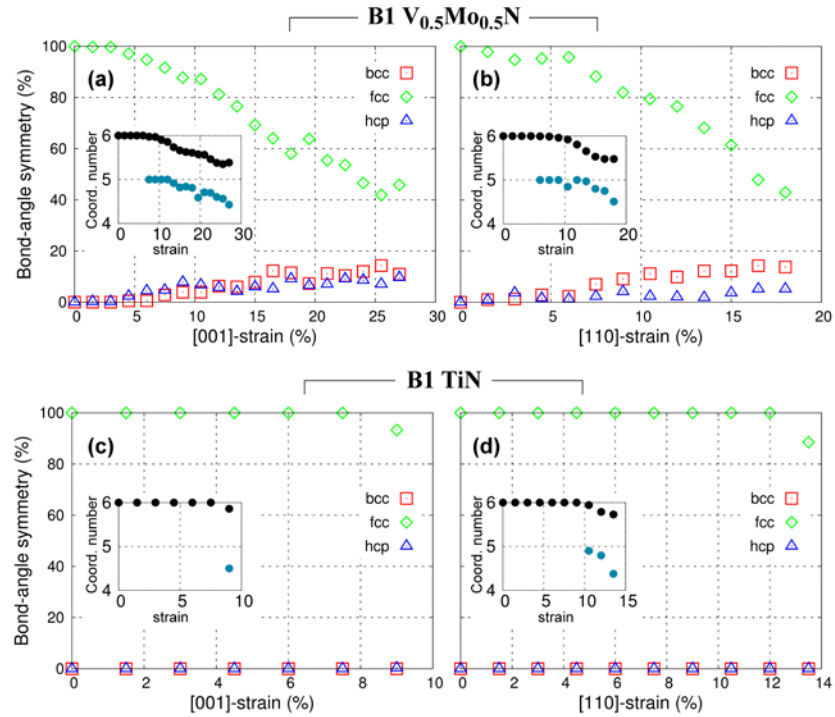


Fig. 7. Percentage of local lattice symmetries (fcc, bcc, and hcp) plotted as a function of tensile strain in VMoN and TiN (computational details are provided in Sec. 2). The insets show the variations in nearest-neighbor atomic coordination numbers averaged over all atoms (black circles) and only for atoms within strongly deformed regions (cyan circles). TiN maintains octahedral fcc-like coordination up to mechanical failure. In contrast, VMoN undergoes gradual structural transformations, which prevent brittle fracture.

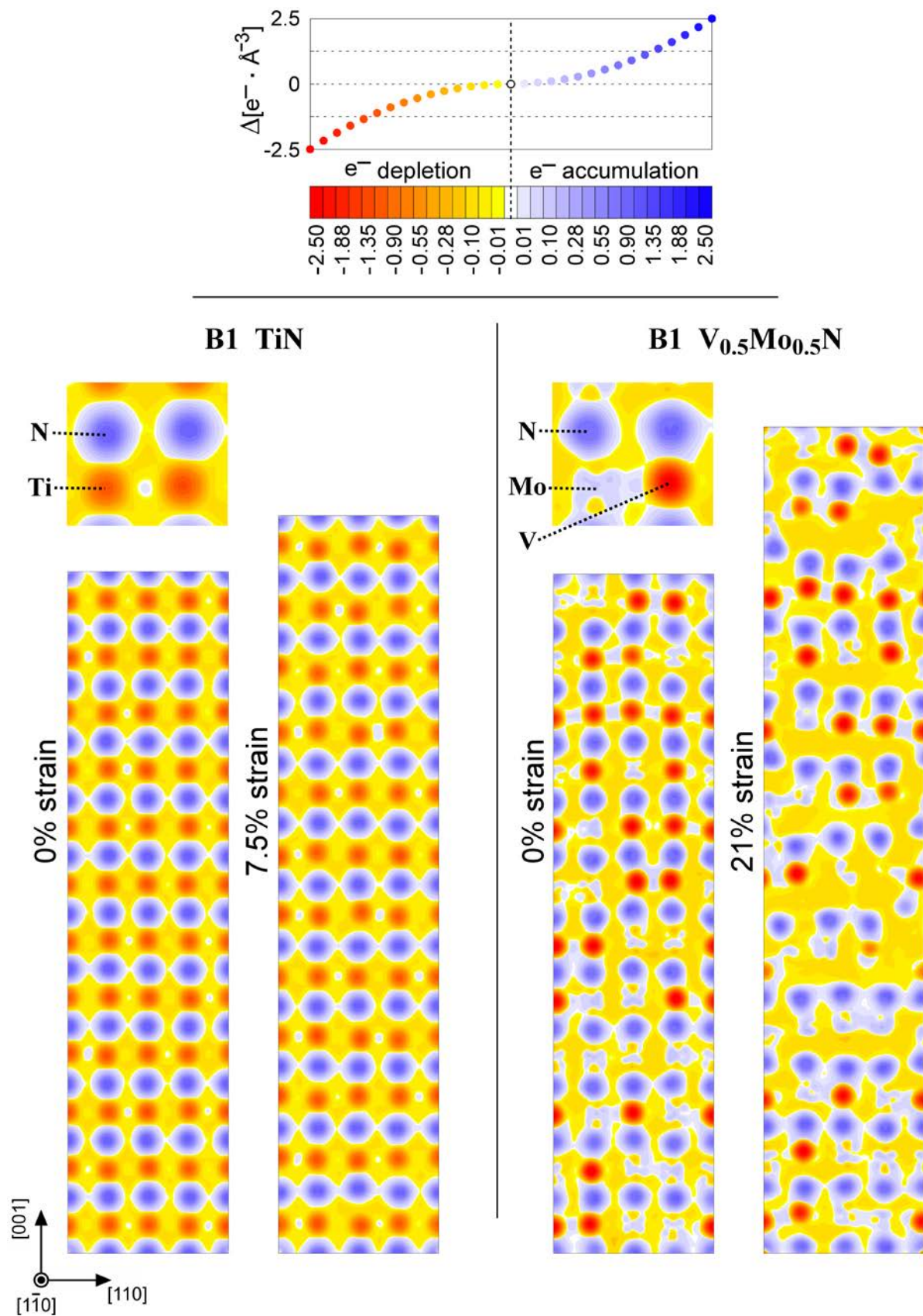


Fig. 8. DFT electron transfer maps determined for AIMD configurations of unstrained TiN(001) and VMoN(001), as well as of [001]-strained TiN(001) and VMoN(001) structures near their breaking points. No significant change is visible in the electronic structure of (primarily ionic) TiN before and after deformation. In contrast, VMoN exhibits a pronounced metallic character, which produces noticeable electron reorganization upon deformation.

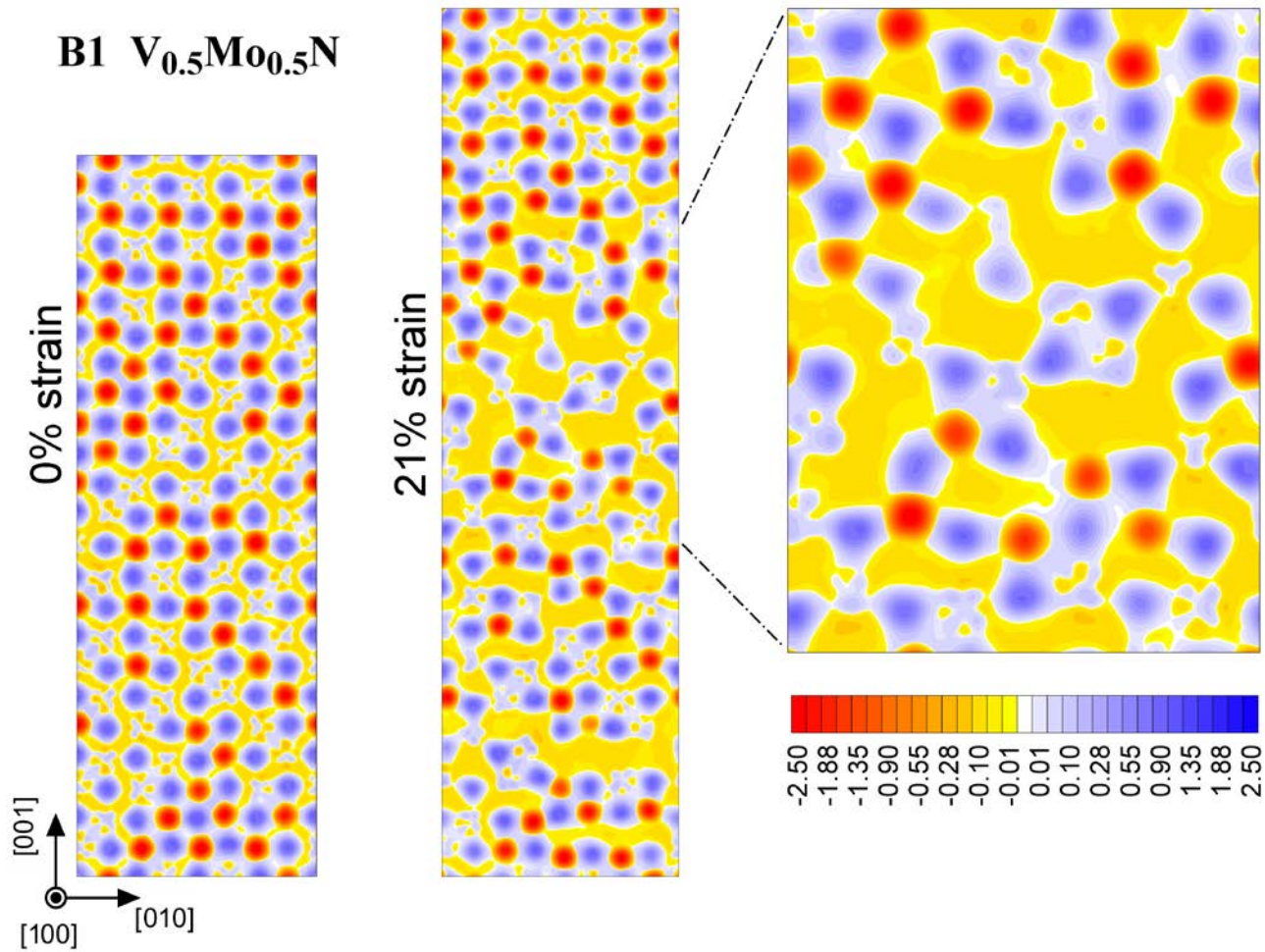


Fig. 9. DFT electron transfer maps [(100) cross section] of unstrained and 21%-strained VMoN(001). The color scale is expressed in $e^- \cdot \text{\AA}^{-3}$. The figure provides an alternative view (in comparison to Fig. 8) of the modifications induced on VMoN chemical bonding by tensile strain.